Effect of Material Inhomogeneity on Thermal Performance of a Rheocast Aluminum Heatsink for Electronics Cooling

Authors: M. Payandeh, I. Belov, A. E. W. Jarfors, M. Wessén

Affiliation: Department of Materials and Manufacturing, School of Engineering, Jönköping University, Box 1026, 551 11 Jönköping, Sweden

Corresponding author: M. Payandeh; Tel.: +46-36-101650; fax: +46-36-166560; email: Mostafa.Payandeh@ju.se

1 Abstract

The relation between microstructural inhomogeneity and thermal conductivity of a rheocast component manufactured from two different aluminum alloys was investigated. The formation of two different primary α-Al particles was observed and related to multistage solidification process during slurry preparation and die cavity filling process. The microstructural inhomogeneity of the component was quantified as the fraction of α_1-Al particles in the primary Al phase. A high fraction of coarse solute-lean α_1-Al particles in the primary Al phase caused a higher thermal conductivity of the component in the near-to-gate region. A Variation in thermal conductivity through the rheocast component of 10% was discovered.

The effect of an inhomogeneous temperature-dependent thermal conductivity on the thermal performance of a large rheocast heatsink for electronics cooling in an operation environment was studied by means of simulation. Design guidelines were developed to account for the thermal performance of heatsinks with inhomogeneous thermal conductivity, as caused by the rheocasting process. Under the modelling assumptions, the simulation results showed over 2.5% improvement in heatsink thermal resistance when the higher conductivity near-to-gate region was located at the top of the heatsink. Assuming homogeneous thermo-physical properties in a rheocast heatsink may lead to greater than 3.5% error in the estimation of maximum thermal resistance of the heatsink. The variation in thermal conductivity within a large rheocast heatsink was found to be important for obtaining of a robust component design.

Keywords: rheocasting, microstructural inhomogeneity, heatsink, thermal conductivity, thermal management, computer simulation.

2 Introduction

A consequence of miniaturization in electronics is that heat dissipation has become an increasingly important factor affecting electronics reliability. Various thermal management techniques to prevent overheating and consequent premature failure have been studied [1]. Common thermal management techniques include solutions such as attaching metal plate-fin heatsinks to high-power electronic components. Material selection for the heatsinks aims to maximize thermal conductivity and minimize both weight and cost, i.e. to achieve the best heat transfer capability per unit mass at lowest possible manufacturing cost.

From an engineering standpoint, in the process of product realization, a high level of co-operation between product development and production is important [2]. Often such a cooperation is restricted in the product design phase due to the lack of established methods capable of considering the effect of manufacturing method on the final properties of components. For instance, in aluminum casting, local variations in the mechanical behavior of a finished component due to the variation of microstructural characteristics can cause deviations from that predicted by finite element simulations based on a homogeneous material description [3].This is often not addressed in robust design of cast components.

The effect of microstructural characteristics on conductive heat transfer in the component is commonly not considered in heatsink design, and thermal conductivity is usually assumed homogeneous throughout the component. In metals such as aluminum and copper, the most common heatsink materials, thermal conductivity depends on the mean free path of electrons [4]. Hence, the microstructure characteristics of the metal become important as all defects in the microstructure can disrupt electron motion and reduce the mean free path, leading to reduced thermal conductivity. Considering the effects of the manufacturing method and alloy selection as two main factors affecting the final microstructure and thereby material properties [5], it is essential to evaluate the influence of the manufacturing process on the heatsink performance.

Today, heatsinks are mainly produced by extrusion, machining or metal casting [6]. Of these processes, casting has a number of advantages compared to the other processes, including cost and freedom to generate complex component geometry [7]. New casting methods such as rheocasting integrated with high-pressure die casting (HPDC) make it possible to improve the heat transfer characteristics of heatsinks. The way towards such an improvement requires both the capability of rheocasting to produce components with complex geometry [8] and the

possibility to cast alloys with reduced concentrations of alloying elements such as Si, Mn, Fe, which are known to adversely affect alloy thermal conductivity [9, 10]. A recent study has shown that rheocast components commonly exhibit inhomogeneous microstructures leading to variations of thermo-physical properties in the rheocast component [11]. This will influence the performance of the heatsink and thus the possibility to maximize the benefits of the rheocasting process. It is therefore necessary to consider inhomogeneous thermo-physical properties in the design phase in order to obtain and optimized thermal performance of the heatsink. This is not required for extruded components, which normally exhibit very homogeneous properties.

Heatsink analysis methods are well developed and the influence of geometry, material selection, surface treatment and airflow conditions on the heat transfer have been investigated [12]. Furthermore, simulation-based heatsink optimization methodologies have been introduced [13]. However, the research in this area mainly relates to the thermal performance optimization of extruded and / or machined heatsinks with homogeneous thermo-physical properties. While temperature dependent behavior is captured, inhomogeneous thermal conductivity resulting from the casting process has not been addressed specifically for Al rheocast heatsinks. In order to evaluate the thermal performance of a rheocast heatsink in an operation environment, the efforts of material/process engineers and the heatsink designers should be coordinated.

The intent of this paper is to determine the relation between inhomogeneous microstructural characteristics and thermal conductivity of a rheocast component, manufactured from two different Al alloys. The inhomogeneous temperature dependent thermal conductivity of two Al alloys is derived to serve as input to heatsink computational fluid dynamics (CFD) models. Furthermore, this paper aims to quantify the effect of inhomogeneous temperature-dependent thermal conductivity on thermal performance of an industrial heatsink in an operation environment, by simulation. The heatsink base-to-ambient thermal resistance is employed to quantify the effect of inhomogeneous thermal conductivity of the heatsink. Finally, conclusions are drawn with the aim to obtain a robust heatsink design process, taking into account inhomogeneous thermal properties of rheocast Al components.

3 Material and Experiments

3.1 Material

A commercial aluminum alloy Stenal Rheo1 and a recently developed low silicon aluminum alloy (Alloy D) were employed in this study, Table 1. Alloy D was designed by reducing the alloying elements that have a significant influence on the thermo-physical properties [9], without significantly compromising castability.

Table 1. Chemical compositions of Stenal Rheo1 and Alloy D (wt. %) and corresponding liquidus temperature.

Alloy	Si	Fe	Cu	Mn	Mg	Zn	Ti	Cr	Al	T_L(°C)
Stenal Rheo1	5.7	0.53	2.2	0.27	0.03	0.72	<0.01	<0.01	Bal.	615
Alloy D	2.4	0.45	0.1	<0.01	0.58	-	-	-	Bal	642

3.2 Rheo-casting and sampling

Experimental work was performed using industrial facilities, including a 400 tons HPDC machine equipped with an automated RheoMetal^{TM} slurry generator [14]. An experimental cavity filter demonstrator for telecom applications, Figure 1, was rheocast. The alloys were prepared in a resistance furnace at a temperature of 675 °C. Ladling was done using a standard cast iron ladle and the shot weight was approximately 5 kg. The **E**nthalpy **E**xchange **M**aterial (EEM) as a cooling agent [15] was immersed into the melt in an amount of 5-6 % of the shot weight while stirring at 900 rpm to generate a slurry with a solid fraction of around 40 %. Directly after completed slurry preparation, a small sample for microstructural investigation was produced by rapid quenching in a chill die.

The die temperature was set to 230-250 °C for the fixed-half and to 280-320 °C for the moving-half. The die cavity filling time was 31 ms with injection speeds of 0.23 and 5.2 m/s for the first and the second phases, respectively. Samples for thermal analysis and microstructure investigation were taken from two different locations of the rheocast component, Figure 1, from the base plate near-to-gate (position 1), and from the base plate near-to-vent (position 2).

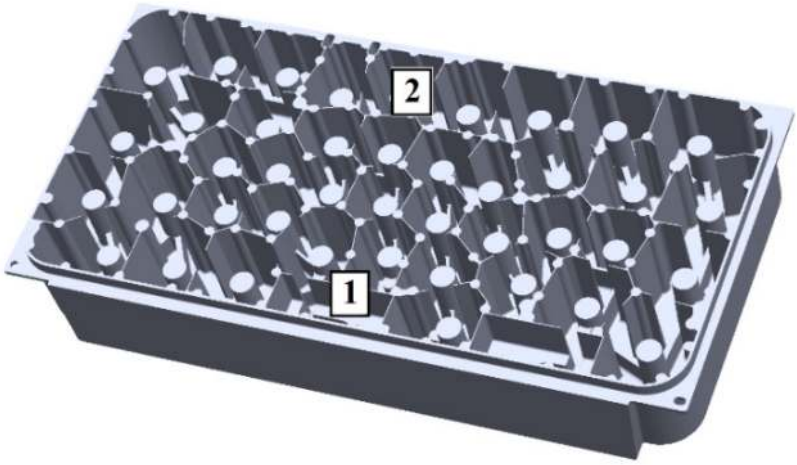

Figure 1. An experimental rheocast cavity filter demonstrator (the numbers indicate sampling positions).

3.3 Microstructural evaluation

In order to determine relationships between microstructural features and thermal conductivity, the samples from positions 1 and 2 were taken for microscopic study. The samples were cut, polished, and etched with a 10 % NaOH etchant. The microstructural observations and quantitative measurements, such as fraction of a phase of interest, were made with Olympus Stream^{TM} image analysis system. Contrast-based recognition and particle size discrimination were employed. Particle size measurements were made for at least six representative images.

The distribution of Si inside the primary Al phase in the samples from position 1 was measured with a scanning electron microscope (SEM) equipped with a wavelength dispersive spectrometer (WDS). The acceleration voltage was 10 kV for Si measurements, using the pure elements as standard.

3.4 Thermo-physical property measurements

A Netzsch LFA 427 laser flash apparatus based on the transient method was used to measure thermal diffusivity $a(T)$ [16]. Thermal diffusivity measurements were performed on cylindrical samples with the diameter 12.5 mm and the height 3.4-3.8 mm. Specific heat $c_p(T)$ was measured with a Netzsch DSC 404C calorimeter and the samples were heated to 500 °C at a rate of 10 °C/min and cooled at a slower rate of 1.5 °C/min before the measurement. Thermal expansion coefficient α was measured with a Netzsch DIL 402C dilatometer. Density ρ at room temperature T_{RT} was determined based on the Archimedes principle and the density at elevated temperatures was obtained from Eq. 1 [17].

$$\rho(T) = \frac{\rho(T_{RT})}{(1-\alpha(T-T_{RT}))^3} \quad (1)$$

The obtained thermo-physical properties served to derive temperature dependent thermal conductivity according to Eq. 2, [18]:

$$k(T)=a(T) \cdot c_p(T) \cdot \rho(T) \quad (2)$$

3.5 Model validation

In order to verify that the obtained thermo-physical properties would lead to correct prediction of heat transfer, a single-fin structure was extracted from the near-to-vent region of the component made of Stenal Rheo1, to represent a single-fin heatsink, Figure 2. A power resistor was screwed to the heatsink base to serve as heat source in the experiment. A thermal paste with thermal conductivity 0.81 W/(m·K) was used as the thermal interface material between the copper base of the resistor and the heatsink. Three K-type thermocouples were glued to the surface of the heatsink at different locations with thermally conductive Ceramix adhesive, Figure 2. One thermocouple was pressed with a screw into the base of the power resistor.

The thermal experiment was conducted at an ambient temperature of 20 ^{o}C in natural convection conditions. The heatsink was placed on an insulating foam. The power dissipation was set to 3.05 W. As a rule, thermal radiation from the heatsink surface is considered in natural convection conditions. A separate set of measurements was conducted to obtain emissivity of the heatsink at different locations. A thermography camera FLIR i5 was employed together with K-type thermocouples to measure the local emissivity at the thermocouple locations.

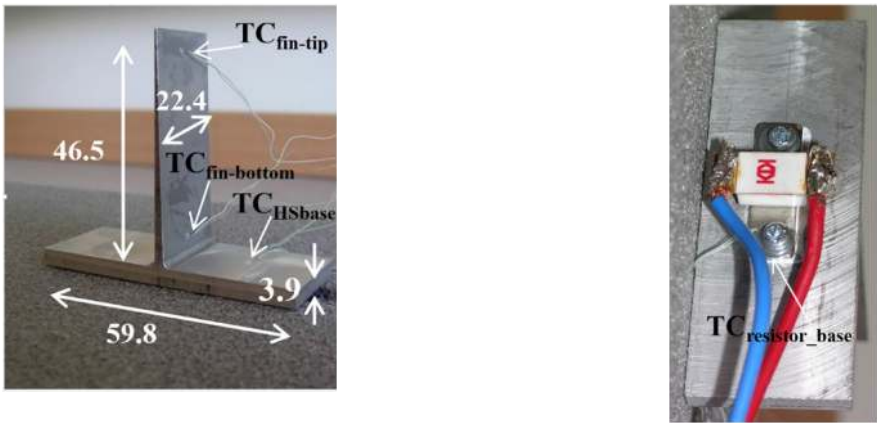

(a) (b)

Figure 2. Experimental setup, including (a) three K-type thermocouples (TC) glued to the surface of the heatsink; (b) power resistor and a K-type thermocouple pressed to the base of the resistor (dimensions in mm).

A transient CFD model of the experimental setup, Figure 3, was created using the simulation tool Flotherm™ from Mentor Graphics. The influence of the screws was neglected, as was the fin tapering. In the model, the fin thickness was set to the average measured fin thickness, i.e. 1.25 mm. The emissivity of the heatsink was set to an average value based on the measured data. In order to take heat conduction through the power cables into account, the power cables were embedded in a single wire of rectangular cross-section. Thermo-physical properties of standard materials in the experimental setup with the single-fin heatsink were taken from standard databases [19]. The properties are collected in Table 2. The computational domain had open boundary faces, and several mesh densities were tested in order to obtain mesh independent results. An algebraic turbulence model was applied [19]. The temperature was monitored in the locations corresponding to the thermocouple locations in the actual experiment.

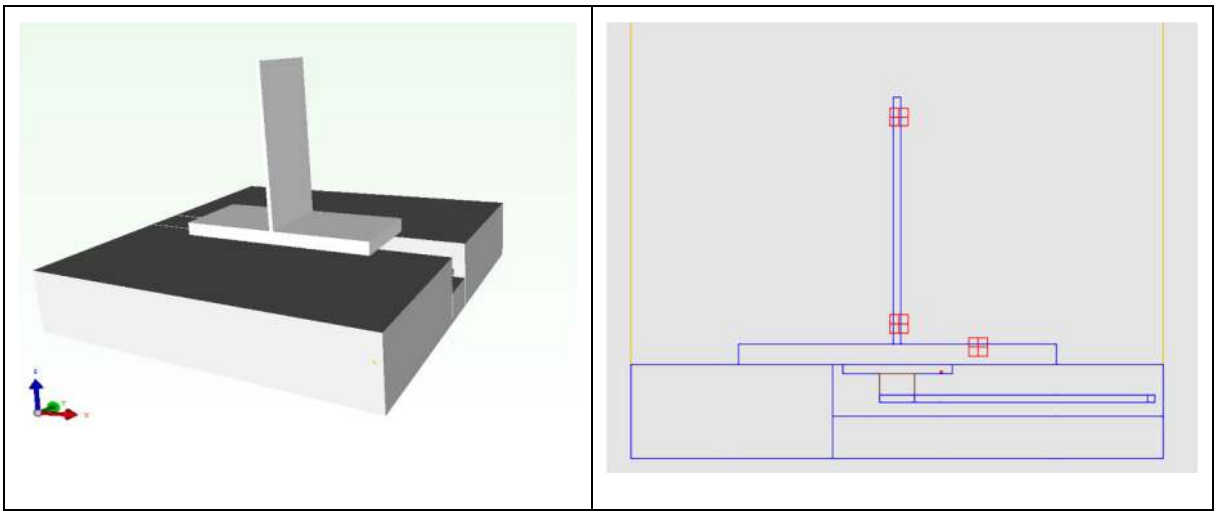

Figure 3. General view of the CFD model of the single-fin heatsink, including monitor point locations (square markers).

Table 2. Thermo-physical properties of materials in the model of the single-fin heatsink.

Material/Part	k, W/(m·°C)	ρ, kg/m^3	c_p, J/(kg·°C)
Copper (cable, resistor base)	386	8930	385
Alumina (resistor body)	16	3970	765
Foam (insulating substrate)	0.05	31	1130

3.6 CFD model of multi-fin heatsink

In order to determine the maximum effect of inhomogeneous thermal conductivity on the thermal performance of a multi-fin heatsink, a series of parametric studies were performed. A steady-state CFD model of an industrial heatsink was developed, Figure 4. The fin height, the average fin width and the central pitch between the fins were set at 150 mm, 1.66 mm and 9.8 mm, respectively. It is worth noting that the outer dimensions of the heatsink corresponded to the outer dimensions of the rheocast cavity filter.

The CFD model for optimization was designed to include two geometrically identical heatsinks HS1 and HS2 separated by an insulator wall in order to prevent heat exchange by radiation between the heatsinks, Figure 4. The ambient temperature for the heatsink operation was set at 65 °C. Natural convection conditions were assumed, with the gravity vector pointing downward along the Y-axis.

Specific heat, density and thermal conductivity of the modeled heatsinks corresponded to the measured properties of Stenal Rheo1 and Alloy D. The computational mesh included 510000 cells. Mesh independent results were obtained. The base of the heatsink was attached to an

insulating substrate, thus only heat conduction in the heatsink was considered. Power electronics components were approximated by heat source objects collapsed towards the base of the heatsink. An approach to simulate various hot spot distributions was developed, which will be discussed later. ~~It is worth noting that minimization of the heatsink base temperature at different power distributions on the heatsink base is out of scope of the present study as is heatsink geometry optimization.~~

3.7 Parametric study

The purpose of the parametric study was to establish thermal resistance variation boundaries for the inhomogeneous rheocast heatsink in relation to a reference heatsink, taking into account different hot spot distributions on the base of the heatsink. This approach can be used in the robust design methodology. It is worth noting that neither minimization of the heatsink base temperature at different hot spot distributions nor optimization of the heatsink geometry is part of the scope.

Emissivity, Al alloy and heatsink base thickness were considered as parameters to define eight optimization scenarios. The oxidized surface emissivity was the average measured emissivity for the single-fin structure and the anodized surface emissivity was 0.8 [19]. The heatsink base thickness was either 3 mm or 8 mm.

The variation of thermal conductivity in the heatsink model resembled the measured inhomogeneous temperature-dependent thermal conductivity of the cavity filter. The parametric study aimed to capture the effect of the inhomogeneity on heat spreading in the heatsink base. Therefore, any variation of microstructure in the direction perpendicular to the base plate of the component (transverse segregation) was not considered. Thus, thermal conductivity of the heatsink in the model did not vary in Z-direction, Figure 4. Inhomogeneous thermal conductivity was addressed through assigning five **M**aterial **P**artitions (MP) in three different **M**aterial **P**artition **A**rrangements (MPA):

(a) Arrangement 1 (MPA1): the material with higher thermal conductivity (MP5) is located on the top of the heatsink and thermal conductivity reduces along the Y-axis in the direction of gravity.
(b) Arrangement 2 (MPA2): the material with lower thermal conductivity (MP1) is located on the top of the heatsink and thermal conductivity increases along the Y-axis in the direction of gravity.

(c) Arrangement 3 (MPA3): the material with the highest homogeneous thermal conductivity (MP5).

Additional simulations showed that five partitions were sufficient to represent inhomogeneous thermal conductivity of the material for the studied heatsink. The density and the specific heat were identical in each material partition. Optimization scenarios are summarized in Table 3.

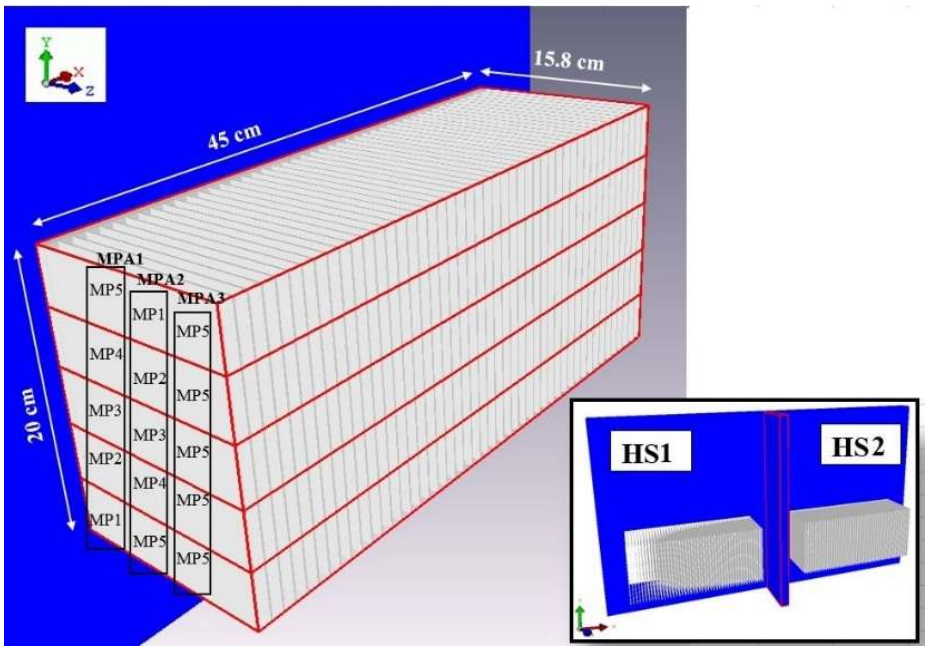

Figure 4. CFD model including two geometrically identical heatsinks (HS1 and HS2) with different thermal properties represented by one of three MPAs; dimensions and material partitions (rectangular borders) are illustrated for one of the heatsinks.

Table 3. Optimization scenarios.

Scenario	Alloy	Surface	Base	MPA1	MPA2	MPA3
A	Stenal Rheo1	Oxidized	8 mm			
B	Stenal Rheo1	Oxidized	8 mm			
C	Alloy D	Oxidized	8 mm			
D	Alloy D	Oxidized	8 mm			
E	Alloy D	Anodized	8 mm			
F	Alloy D	Anodized	8 mm			
G	Alloy D	Oxidized	3 mm			
H	Alloy D	Oxidized	3 mm			

As the performance of a heatsink is significantly dependent on the hot spot distribution on the heatsink base, an array of 15 heat sources was introduced, Figure 5. The arrangement of hot

spots was considered as a design parameter in each optimization scenario. Optimization was carried out using the *sequential optimization method* [13]. Sequential optimization is a local optimization technique dealing with time-consuming CFD simulations without reliance on derivative information. Local linear approximations of the model outputs are obtained via weighted regression. Next, the approximate models are optimized within a trust region centered on the current best design. A new local linear approximation is built at each iteration. Thereby, a new design is evaluated, in order to improve the objective function. Alternatively, the trust region is decreased [13].

Each scenario consisted of designs with different heat source arrangements. Heat sources with reference numbers 4 to 12 were varied between 0 and 70 W in the optimization scenarios, whereas the heat sources along the vertical sides (reference numbers 1-3 and 13-15) were set to 1 W. The highest power dissipation in the central part of the heatsink base agrees well with current electronics design and thermal management practices. The total heat dissipation for each heatsink did not exceed 300 W, according to the industrial specification. Furthermore, the distribution of the heat sources in HS1 was mirrored in the HS2, Figure 5, in order to reach identical radiation heat-exchange conditions with the ambient environment.

Initial designs for optimization represented by hot spot distributions were generated with Latin Hyper Cube Design of Experiment (DoE) method [20]. At least 75 designs were generated for each optimization scenario. The optimization was performed from several best DoE designs. This would ensure relatively good coverage of the design space and determination of the objective function values close to the global optimum. An example of selected hot spot distributions generated in the DoE and optimization process is provided in the cumulative diagram, Figure 5. In the cumulative diagram, the heat sources are represented by columns of different colors placed on the top of each other. It allows estimation of power contribution of each heat source to the total power dissipated on the heatsink base.

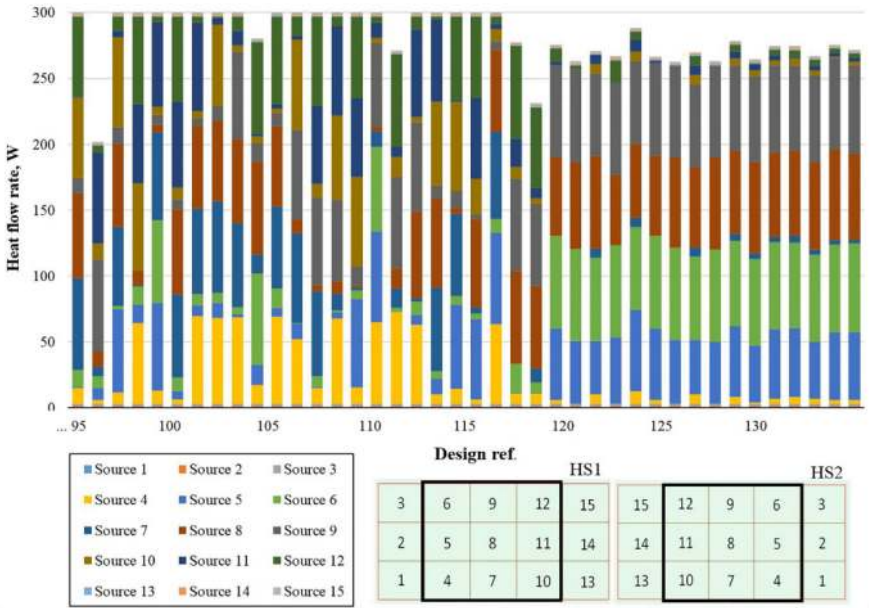

Figure 5. Array of heat sources with reference numbers from 1 to 15, attached to the heatsink base - example of hot spot distributions investigated in scenario C: heat sources marked with the black frame were varied in the optimization process.

The *maximum temperature of heatsinks* ($T_{max,HS1}$ and $T_{max,HS2}$) was monitored in the simulations. The objective function to maximize was the difference between the maximum temperatures of the heatsinks at similar hot spot distributions:

$$f_{obj} = T_{max,HS1} - T_{max,HS2} \quad (3)$$

The maximum temperature of the heatsink base was constrained to stay below 110 ºC, according to the industrial specification. Material arrangements MPA2 and MPA3 were assigned to HS1 and HS2, respectively, in scenarios A, C, E, and G. In scenarios B, D, F, and H, MPA2 and MPA1 were assigned to HS1 and HS2, respectively.

From the engineering perspective, it is more instructive to quantify the maximum thermal resistance between the hottest point in the base of heatsink and the ambient environment (T_{amb}=65 ºC), since the temperature of the hottest point corresponds approximately to the case temperature of an electronic component attached to the base of the heatsink. Therefore, the percentage difference ($\%R$) defined as

$$\%R = 100 \times \left(1 - \frac{T_{max,HS2} - T_{amb}}{T_{max,HS1} - T_{amb}}\right) \quad (4)$$

indicates the thermal resistance improvement/degradation when comparing heatsinks HS1 and HS2, at the same hot spot distribution.

4 Results and discussion

4.1 Microstructural Features

A microstructural investigation of samples taken from position 1 and position 2 was carried out on both alloys. Figure 6(a) shows a typical microstructure of Stenal Rheo1 in the as-rheocast condition. The microstructure of the alloy consisted of relatively coarse globular α-Al phases (referred to as α_1-Al particles). Alloy D revealed similar microstructural features. The diameter of the α_1-Al particles ranged from 50 μm to 70 μm. A study performed on the quenched slurry samples showed that the α_1-Al particles were formed during slurry preparation; hence during the step when the temperature of the melt was reduced down to the final slurry temperature.

Furthermore, the microstructure also contained fine α-Al phases (referred to as α_2-Al particles). The diameter of the α_2-Al particles ranged between 10 μm and 25 μm. The formation of α_2-Al particles is related to solidification of the liquid portion of the slurry after injection into the die cavity at a higher cooling rate and in the absence of significant shear force. This was confirmed by observing α_2-Al particles only in the final component and not in the quenched slurry sample. A similar behavior of the remaining liquid solidification was reported earlier [21]. The results of that study showed the possibility of having discrete nucleation inside the die cavity to form α_2-Al particles through heterogeneous nucleation.

The Al-Si eutectic phase and Al_2Cu-bearing phase precipitated in the regions between α-Al phases below the eutectic temperature of Stenal Rheo1. Similarly, the formation of Fe-rich intermetallic compounds together with Al-Si eutectic phase was observed in Alloy D. Based on the composition of the original melt, the sequence of solidification (primary phase and eutectic reaction) was calculated using JMatPro^{TM} [22, 23]. According to the calculated results needle-shaped β(AlFeSi) was the most favorable eutectic phase in Alloy D and formed before the eutectic Si phase. The JMatPro^{TM} calculation showed a good agreement with microstructural evaluation of Alloy D where the presence of β(AlFeSi) was observed together with the Al-Si eutectic phase, Figure 6(b).

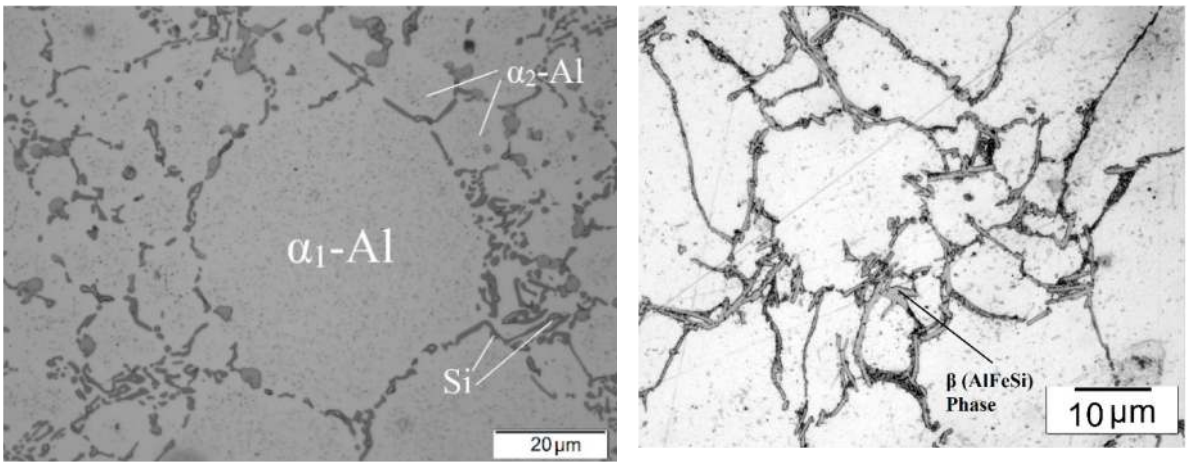

(a) (b)

Figure 6. Optical micrographs of (a) microstructure of the Stenal Rheo1 component and (b) β (AlFeSi) phase in Alloy D.

The concentration of Si in four α_1-Al particles was measured by WDS at the center, mid-radius and full radius for Stenal Rheo1 and Alloy D, Figure 7(a). Six α_2-Al particles were measured at the center and full radius, Figure 7(b). The Si concentration profile showed a homogenous segregation inside the α_1-Al particles for both alloys, Figure 7(a). This may be a consequence of Si diffusion and homogenization within the α_1-Al particles during slurry preparation at the slurry temperature. This was proven by comparing the measured Si concentration with the solubility of Si in Al at the slurry temperature. The Si solubility was calculated by means of the JMatPro^{TM} software with Al-DATA database, for both alloys [22, 23]. The α_2-Al particles had higher concentrations of alloying elements compared to α_1-Al particles, Figure 7(b). This also proved that the α_2-Al particles formed in a different nucleation event at a lower temperature, inside the die cavity [21].

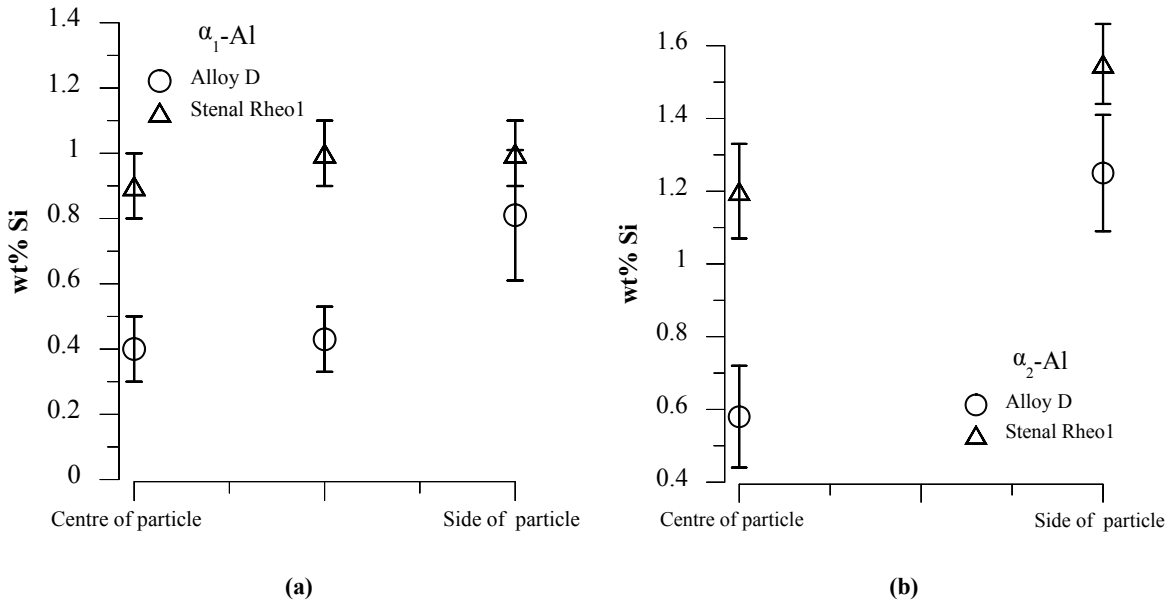

Figure 7. Measured concentration of Si in (a) α_1-Al particles (b) α_2-Al particles for both Stenal Rheo1 and Alloy D.

The microstructure of samples from positions 1 and 2 was studied. Figure 8(a) and Figure 8(b) show the microstructural features at position 1 for Stenal Rheo1 and for Alloy D, respectively, with a larger fraction of α_1-Al particles compared to α_2-Al particles. Furthermore, Figure 9(a) and Figure 9 (b) show the microstructural features at position 2, which contained a larger fraction of α_2-Al particles as well as porosity related to air entrapment. As the primary Al phase in the microstructure of the rheocast alloys consisted of solute-lean α_1-Al and solute-rich α_2-Al particles, the microstructural inhomogeneity was quantified as the fraction of α_1-Al particles in the primary Al phase, see Table 4. The results indicated a level of macrosegregation through the components for both alloys. However, the same difference in fractions of α_1-Al particles was observed between the two positions.

Table 4. Fraction of α_1-Al particles in the microstructure of sample in different positions.

	fs, % (Alloy D)	fs, % (Stenal Rheo1)
pos1- base plate	66±4	72±6
pos2 – base plate	22±6	27±4

The inhomogeneity of microstructure can be explained by a separation of the liquid and solid portions of the slurry during the injection process. It is likely that the liquid portion of the slurry as the higher mobility phase was preferentially forced into the gating system and injected into the cavity in advance of the solid portion of the slurry. During the later stages of injection, the portion of slurry that contained a larger fraction of α_1-Al particles together with some entrapped melt was pushed into the near-to-gate region. Kaufman *et al.* [24] found the same type of separation of the liquid and solid portions of the slurry in a SSM-HPDC component and explained it by a so-called sponge effect. This phenomenon occurs during injection, where the solute-enriched liquid portion of slurry squeezes out, leaving the solid phase behind. The formation of porosity at position 2 is related to the lower viscosity of the liquid portion of the slurry and transition of liquid flow to a turbulent mode due to increase of the Reynolds number.

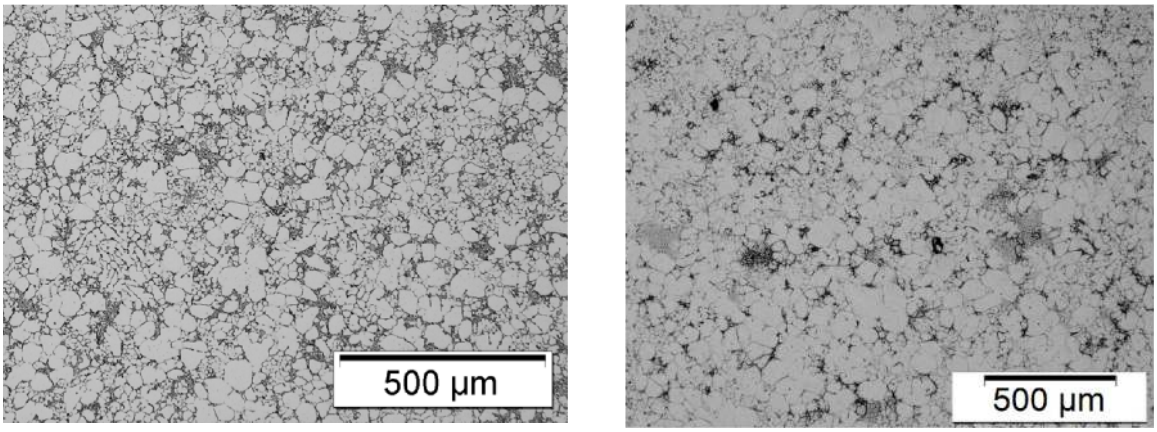

(a) (b)

Figure 8. Microstructure of the components in position 1: (a) Stenal Rheo1 and (b) Alloy D.

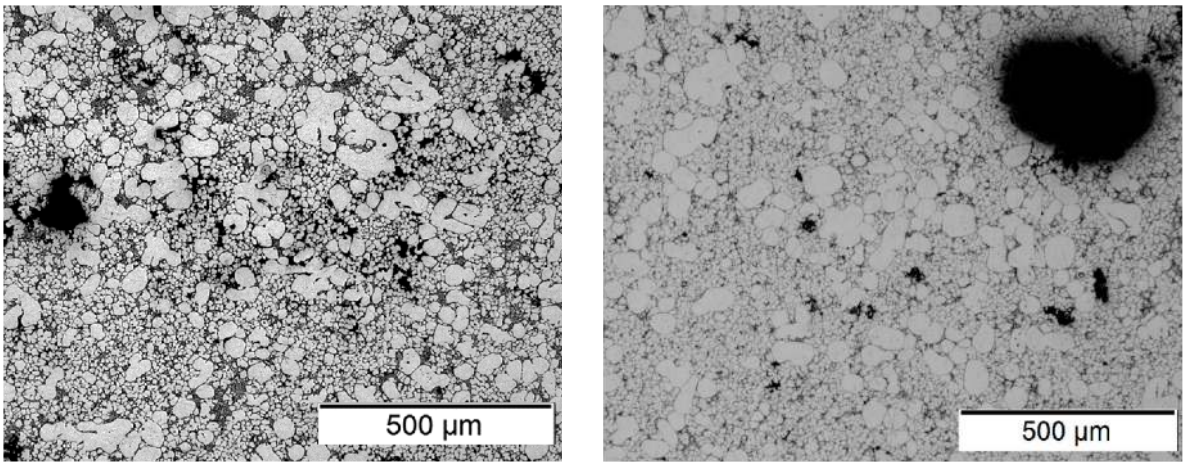

(a) (b)

Figure 9. Microstructure of the components in position 2: (a) Stenal Rheo1 and (b) Alloy D.

4.2 Thermo-physical properties

The apparent (average) specific heat was measured. The energy absorbed or released due to dissolution and precipitation events during heating was excluded from the data by means of curve fitting for the temperature region 100-250 °C. The specific heat was extrapolated from the fitted curve. The specific heat data is presented in Table 5.

Table 5. The measured apparent specific heat for Stenal Rheo1 and Alloy D.

Temperature, °C	c_p, J/(kg·°C) Stenal Rheo1	c_p, J/(kg·°C) Alloy D
30	885±1	899±9
100	909±1	921±9
150	930±10	942±10
200	948±10	960±10
250	966±10	976±10
300	986±12	993±12
350	1004±12	1010±12

The density of Stenal Rheo1 and Alloy D at room temperature was measured as 2700 kg/m^3 and 2680 kg/m^3, respectively. The coefficient of thermal expansion (CTE) for different temperature ranges are collected in Table 6. Three temperature intervals were considered for measurement, as both alloys showed an increase in thermal expansion starting at 210-220 °C. The average values were used to calculate the density at elevated temperatures, according to Eq. 1.

Table 6. CTE for Stenal Rheo1 and Alloy D.

Temperature interval,°C	CTE, ppm/°C Stenal Rheo1	CTE, ppm/°C Alloy D
30-200	24.6±0.2	23.6±0.8
200-315	33.3±0.5	29.1±0.4
315-430	23.8±1.0	23.9±0.7

Thermal diffusivity of Stenal Rheo1 and Alloy D was measured during heating from 30 °C to 400 °C, at positions 1 and 2 of the component. The thermal diffusivity values presented in Figure 10(a) are the average of five measurements at each temperature. The results indicate that Alloy D had a higher thermal diffusivity as compared to Stenal Rheo1 in both positions. Furthermore, inhomogeneous thermal diffusivity was observed within the rheocast component, with a higher thermal diffusivity measured at position 1 (base plate near-to-gate), compared to position 2 (base plate near-to-vent). The difference in thermal diffusivity started to decrease when the samples were at temperatures above 200 °C. Thermal conductivity was calculated from Eq. 2 based on the measured thermal diffusivity, specific heat and CTE, as presented in Figure 10(b). It reveals 5% and 10% difference in thermal conductivity between the near-to-gate and near-to-vent regions of the component made of Stenal Rheo 1 and Alloy D, respectively, at the intended operation temperature 100°C.

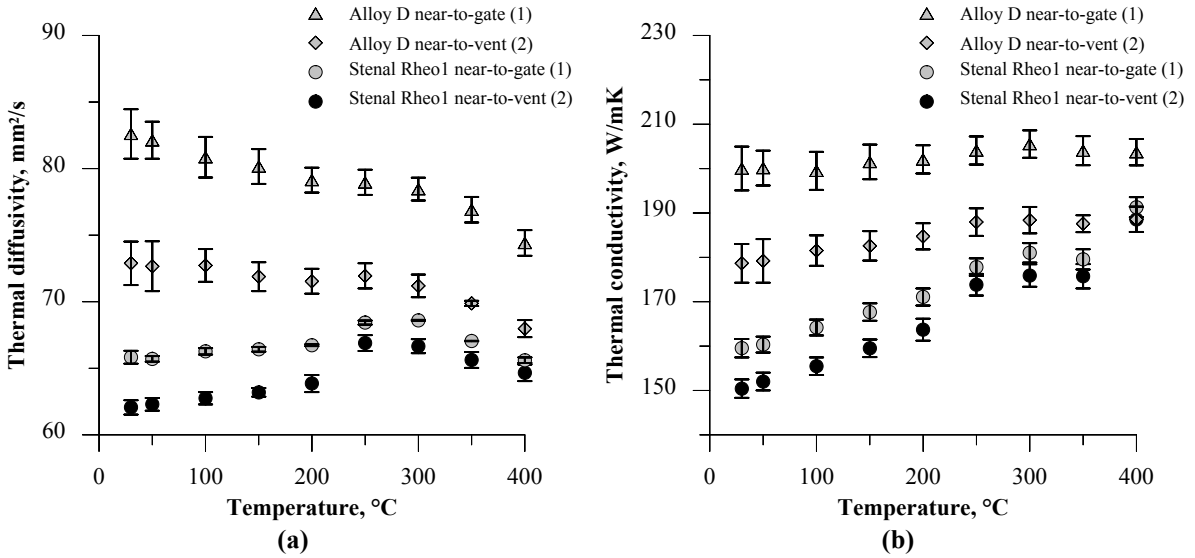

Figure 10. (a) Measured thermal diffusivity and (b) derived thermal conductivity for both Stenal Rheo1 and Alloy D.

4.3 Relation between microstructure and thermal conductivity

The microstructural investigation revealed that both alloys consisted of coarse α_1-Al particles formed during slurry preparation and fine α_2-Al particles formed during secondary solidification in the die cavity. The secondary solidification occurred at lower temperatures, where the solubility of Si and Cu in the α_2-Al particles is higher. The macrosegregation level was evaluated as the difference between the fraction of α_1-Al and α_2-Al particles in different regions of the rheocast components. It was confirmed that the regions with a larger amount of α_1-Al particles, Table 4, had a higher thermal conductivity, Figure 10.

The relation between microstructural characteristics and thermal conductivity is ascribed to the effect of the different phases in the microstructure on the mean free path of electrons [4]. The electron mean free path is strongly decreased by lattice perturbations such as impurities, solutes, vacancies, and dislocations. Atoms in solid solution have the greatest influence on thermal conductivity as they form a large number of scattering centers in the matrix. This is more critical when a highly conductive phase such as aluminum forms a primary phase (matrix) and alloy elements such as Si, or Cu precipitate as solid solutions in the matrix. The ability of lattice disturbances to scatter electrons depends both on the particular alloying elements and on the concentration of these elements. Therefore, percolation of electrons in an inhomogeneous microstructure depends on the characteristics of the conducting phases and their volume fraction. Moreover, despite the presence of scattering sites for free path of electrons, the magnitude of the interaction between electrons and the impurities depends both on the

difference in electronic configuration between the solute and the solvent and on how much the impurities disturb the lattice.

The results from WDS measurements confirmed a higher concentration of dissolved elements in α_2-Al particles as compared to α_1-Al particles. This is in good agreement with the findings from the solidification sequence where α_2-Al particles formed at a lower temperature than α_1-Al particles. Since α_1-Al particles have higher thermal conductivity as compared to α_2-Al, the greater fraction of α_1-Al particles in position 1 would improve thermal conductivity of this region. The results in Table 4 show that the fraction of α_1-Al particles in position 2 is approximately one-third of that in position 1. Similarly, a larger fraction of α_2-Al particles in position 2 would indicate a decrease in the amount of conductive phase and thus a significant reduction of the mean free path of electrons, leading to a lower thermal conductivity in this region of the component.

The effect of solute in the matrix on thermal conductivity is weakened in the temperature range between 200 ^{o}C and 300 ^{o}C, Figure 10, where the dissolved elements start to precipitate. The precipitation results in a decreased number of disturbance sites in the matrix and thereby in increased thermal conductivity. Since the material in position 2 contained more solute-rich α_2-Al particles compared to position 1, a larger rate of increase of thermal conductivity was observed in position 2. This phenomenon was more pronounced for Stenal Rheo1 compared to Alloy D as the former had a higher concentration of dissolved elements in the aluminum matrix, Figure 7.

A similar trend in concentration of α_1-Al particles was observed in the direction from the gate to the vent for the components made of Stenal Rheo 1 and Alloy D. This suggests similar differences in the thermal conductivity between near-to-gate and near-to-vent regions can be expected for both alloys. However, the difference in thermal conductivity between these regions was larger for Alloy D, i.e. 10% compared to 5% for Stenal Rheo1. This can be explained e.g. by a pronounced tendency to formation of interdendritic shrinkage porosity in Alloy D [25].

4.4 Incorporation of local thermo-physical properties in the model

The values of thermal conductivity measured at different positions of the component, Figure 10(b), depend both on the temperature and on the microstructure. The microstructure of the alloys changes from the near-to-gate to the near-to-vent regions. In order to utilize the measured data in a heatsink simulation model with gate-to-vent distance similar to the rheocast cavity filter, linear interpolation was applied.

Temperature dependent thermal conductivity of the material was derived from the measurement data by curve fitting in the temperature range of interest, from 30 ºC to 150 ºC, Figure 11. The obtained $k(T)$ functions from the near-to-gate and near-to-vent regions were assigned to material partitions MP5 and MP1, respectively. The temperature dependent thermal conductivity $k(T,MP_i)$ for material partitions MP2 to MP4 was approximated with linear interpolation between MP1 and MP5, for Stenal Rheo1:

$$k(T, MP_i)= (0.076-0.001\cdot MP_i)\cdot T+2\cdot MP_i +145.8, \quad (5)$$

and for Alloy D:

$$k(T, MP_i)= (0.04-0.006\cdot MP_i)\cdot T+6\cdot MP_i +169.85. \quad (6)$$

where i and T vary from 1 to 5 and from 30 ºC to 150º C, respectively. The alloy density variation in this temperature range was negligible. Therefore, the densities of Stenal Rheo1 and Alloy D were assumed to be temperature independent in the model and set at 2700 kg/m^3 and 2680 kg/m^3, respectively. The same observation held for specific heat (c_p), which was set at 900 J/(kg·ºC) for both alloys.

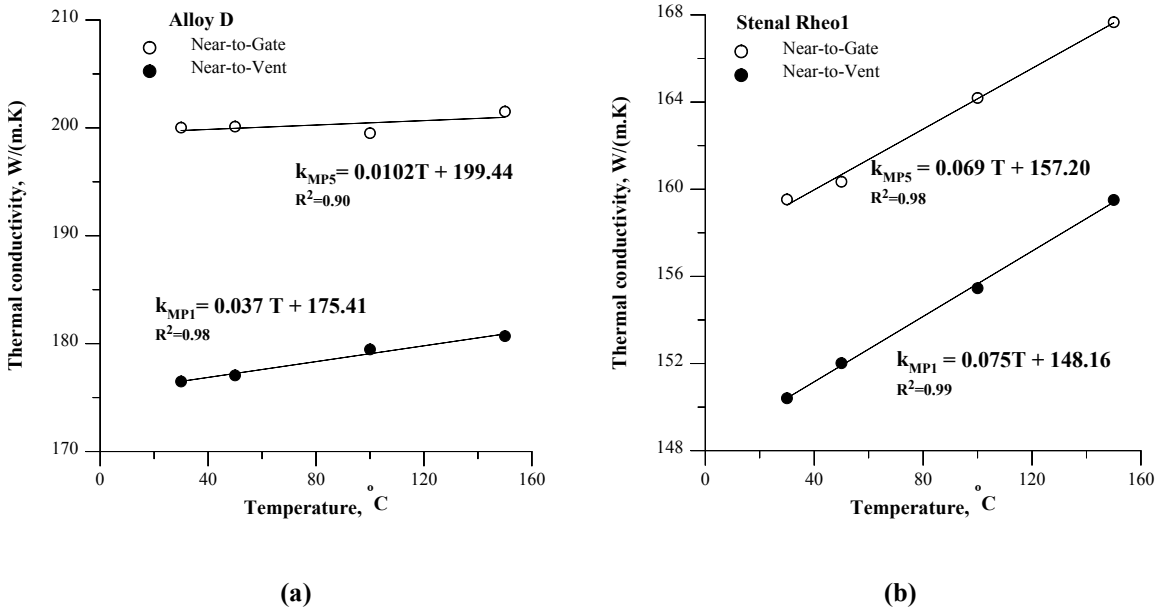

Figure 11. Temperature dependent thermal conductivity of the alloys derived from the measurement data (points) by linear fitting (solid line): (a) Alloys D (b) Stenal Rheo1.

4.5 Validation of single-fin heatsink model

Since the single-fin structure was extracted from the vent region of the Stenal Rheo1 cast component, thermo-physical properties of MP1 were assigned to the single-fin heatsink in the

model. The results of emissivity measurements for the oxidized surface of the single-fin heatsink are provided in Table 7, for three locations, Figure 2. The average value 0.22 was used in the model for the oxidized surface of the heatsink.

Table 7. Emissivity measurements for the oxidized surface.

Measurement localization	Surface emissivity
Fin tip	0.15
Fin bottom	0.30
HS base	0.20
Average	0.22

The results of transient model validation are provided in Figure 12. A general agreement was achieved for all the monitored locations. The temperature rise above the ambient temperature was the validation metric. The largest difference between the simulation and the measurement was observed on the fin-tip. The average percentage difference was around 3%, whereas the maximum difference in the steady state conditions was less than 2%. This agreement between the CFD modeling and experimental results established a link between the measured thermo-physical properties and the heat transfer characteristics of the component, and validates the modelling method for temperature predictions. The simulation results increased confidence in the material and surface characterization methods employed to deliver the thermo-physical and surface properties of interest.

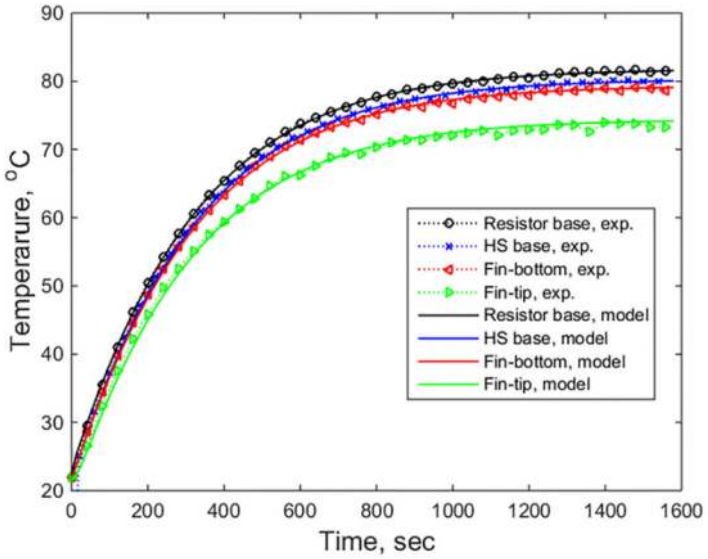

Figure 12. Model validation results for single-fin structure.

4.6 *Parametric study of industrial heatsink*

The optimization scenarios according to Table 3 were realized. In the simulated scenarios, heatsinks with MPA2 delivered the highest maximum temperatures followed by heatsinks with MPA1. Heatsinks with MPA3 having the highest homogeneous thermal conductivity always resulted in the lowest maximum temperature, at equivalent hot spot distributions. An example of temperature distribution on the base of HS1 and HS2 is shown in Figure 13, for a design from scenario C.

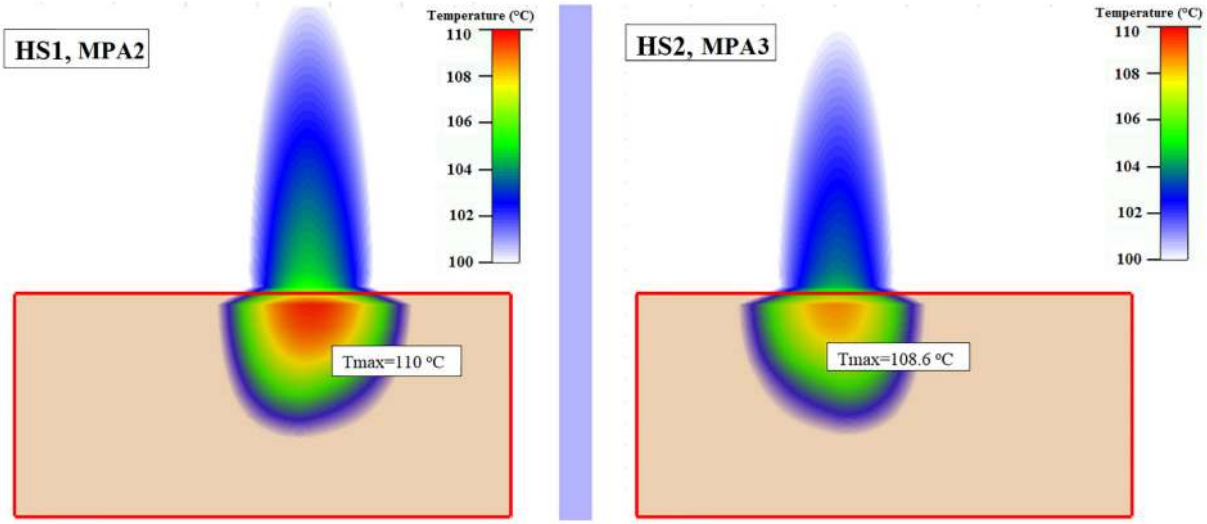

Figure 13. Temperature distribution on the base of HS1 and HS2.

The detailed results for the heatsink maximum temperature and corresponding objective function, Eq. 3, for scenario C are shown in Figure 14. The designs with large heat sources concentrated towards the top edge of the heatsink exhibited the strongest effect of the inhomogeneous thermal conductivity. The T_{max} value for the heatsink HS1 with inhomogeneous material arrangement MPA2 was as expected higher than for the heatsink HS2 with MPA3.

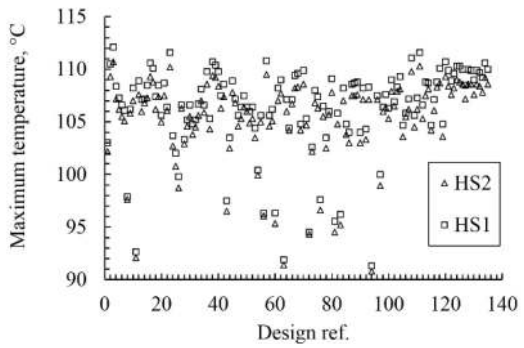

(a)

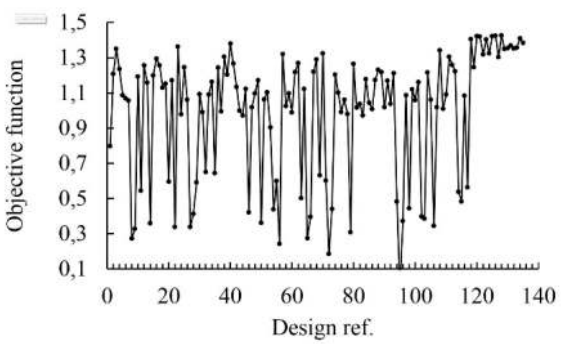

(b)

Figure 14. (a) Maximum temperatures and (b) evolution of the objective function values in scenario C.

The temperature difference and the percentage difference in the maximum thermal resistance, Eq. 4, for optimization scenarios A-H are summarized in Table 8. As an example, for scenario A, the maximum base-to-ambient thermal resistance of the heatsink made of inhomogeneous Stenal Rheo1 alloy was for some hot spot distributions 1.7% higher than the corresponding thermal resistance of the heatsink made of homogeneous Stenal Rheo1. The effect of orientation of the inhomogeneous heatsink with respect to gravity on the heatsink thermal performance (scenario B) was somewhat lower than in scenario A for the same alloy. The calculated percentage difference in thermal resistance was 1.2%.

Similar comparisons made for Alloy D revealed 3.3% difference in thermal resistance between heatsink with MPA2 and heatsink with MPA3 (scenario C) and 2.4% difference between heatsink with MPA1 and heatsink with MPA2 (scenario D). Next, the results for the simulation scenarios E and F (anodized surface) were almost identical to the results for scenarios C and D (oxidized surface). Thus, variation of emissivity from 0.22 to 0.8 neither enhanced nor weakened the effect of inhomogeneous thermal conductivity on the heatsink performance.

Similarly, the effect of inhomogeneous thermal conductivity was evaluated for the heatsinks with thin base (3 mm) in scenarios G and H. The effect was found to be somewhat higher when compared to scenarios C and D, where the heatsinks with base thickness 8 mm were studied.

Table 8. Summary of results from different optimization scenarios.

Scenario	A	B	C	D	E	F	G	H
f_{obj}**,°C**	0.7	0.5	1.4	1.0	1.4	0.9	1.6	1.1
R, %	1.7	1.2	3.3	2.4	3.2	2.2	3.6	2.6

5 Conclusion

The relation between inhomogeneous microstructure and thermal conductivity of a rheocast Al component was investigated in order to establish methods, to be used during the design phase of heatsinks for electronics cooling, which can account for property variations in the part. The microstructural analysis of the rheocast components revealed that coarse solute-lean α_1-Al particles formed during slurry preparation and that fine solute-rich α_2-Al particles formed during solidification in the die cavity. It was found that the thermal conductivity varied strongly between different parts of the component. In the region near-to-vent the thermal conductivity was lower than in the region near-to-gate.

A strong relation exists between the fraction of high conductivity phases (α_1-Al particles) and thermal conductivity of Stenal Rheo 1 and Alloy D. The fraction of α_1-Al particles near-to-vent was approximately one-third of that near-to-gate for both alloys. This resulted in 5% and 10% difference in thermal conductivity between the gate and vent regions of the component made of Stenal Rheo 1 and Alloy D respectively, at the operation temperature of interest, 100^{o}C.

The effect of inhomogeneous thermal conductivity on the aluminum heatsink performance was studied by simulation. The measured thermo-physical properties were incorporated both in the transient CFD model of a single-fin heatsink and in the steady-state model of an industrial multi-fin heatsink. The multi-fin heatsink had the gate-to-vent distance similar to the rheocast component and thus inhomogeneous thermal conductivity determined by the measurements was assumed. The transient CFD model of the single-fin heatsink was experimentally validated within 3%.

The optimization methodology was developed to determine the maximum influence of inhomogeneous thermal conductivity on the thermal performance of the multi-fin heatsink. Taking into account the modeling assumptions, the following design guidelines link the thermal performance of cast Al heatsinks with the inhomogeneous thermal conductivity caused by the rheocasting process.

Inhomogeneous thermal conductivity in the large heatsinks should be considered in the heatsink design phase, especially for rheocast components made of Alloy D. Neglecting the influence of inhomogeneous thermal conductivity may lead to over 3.5% error in estimation of the maximum thermal resistance of the heatsink (base-to-ambient). A 2.5% improvement in heatsink thermal resistance can be achieved when the alloy with higher thermal conductivity prevailing in the near-to-gate region is located on the top of the heatsink, and the fins are aligned

with gravity. Thus, orientation of inhomogeneous heatsink along the gravity direction must correlate with the location of the gating system in the rheocasting process. The effect of inhomogeneous thermal conductivity is independent of the emissivity of the heatsink, and depends only weakly on the base thickness.

These results also confirm the importance of communication between the heatsink process / material engineers and electronics designers in the product design phase, which will help to improve the accuracy of heatsink performance estimation.

6 Acknowledgements

This work is supported by the KK-foundation (RheoCom Project no. 20100203), which is gratefully acknowledged. The authors would like to thank COMPtech AB for the supply of materials and cast components. Huawei Technologies' Sweden AB are acknowledged for help and technical support.

7 References

[1] R. C. Chu, R.E. Simons, M.J. Ellsworth, R.R. Schmidt, V. Cozzolino, Review of cooling technologies for computer products, Device and Materials Reliability, IEEE Transactions on 2004, 4(4), pp. 568-585.

[2] M. Tomovic, and S. Wang, Product Realization: A Comprehensive Approach. 2008: Springer US.

[3] J. Olofsson, and I.L. Svensson, Closed chain simulations of a cast aluminium component-Incorporating casting process simulation and local material characterization into stress-strain simulations. ISIJ international, 2014. 54(2): pp. 259-265.

[4] A. A. Abrikosov, A. Beknazarov, Fundamentals of the Theory of Metals. vol. 1, Amsterdam: North-Holland, 1988.

[5] J. G. Kaufman, L. R. Elwin, Aluminum alloy castings: properties, processes, and applications. ASM International, Materials Park, OH 44073-0002, 2004.

[6] K. Azar, B. Tavassoli, Qpedia Thermal Management–Electronics Cooling Book, vol. 2. Advanced Thermal Solutions, 2008.

[7] K. P. Keller, Cast heatsink design advantages, Thermal and Thermomechanical Phenomena in Electronic Systems. The Sixth Intersociety Conf. ITHERM'98, 27-30 May, Seattle, Washington, USA, 1998, pp. 112-117.

[8] M. Wessén, Rheogjutning av extremt tunnväggiga komponenter, Aluminium Scandinavia, No. 12012, pp. 16-17.

[9] P. Olafsson, R. Sandstrom, Å. Karlsson, Comparison of experimental, calculated and observed values for electrical and thermal conductivity of aluminium alloys, J. Mater. Sci. 1997, 32(16), pp. 4383-4390.

[10] T. Grimmig, A. Ovcharov, C. Afrath, M. Bünck, A. Bührig-Polaczek, Potential of the rheocasting process, demonstrated on different aluminum based alloy systems, Solid State Phenomena, 2006, vol. 116, pp. 484-488.

[11] M. Payandeh, Rheocasting of Aluminium Alloys: Slurry Formation, Microstructure, and Properties, Licentiate thesis, Dissertation series No. 6, Jönköping University, Jönköping, 2015.

[12] A. Bar-Cohen, M. Iyengar, A. D. Kraus, Design of optimum plate-fin natural convective heat sinks, J. Electronic Packaging, 2003, 125(2), pp. 208-216.

[13] J. Parry, R.B. Bornoff, P. Stehouwer, L.T. Driessen, E. Stinstra, Simulation-based design optimization methodologies applied to CFD, Components and Packaging Technologies, IEEE Transactions on, 2004, 27(2), pp. 391-397.

[14] M. Wessén, H. Cao, The RSF technology, A possible breakthrough for semi-solid casting processes. Int. Conf. of High Tech. Die Casting, 21 – 22 September, Vicenza, Italy, 2006.

[15] M. Payandeh, A. E. W. Jarfors, and M. Wessén. Effect of superheat on melting rate of EEM of Al alloys during stirring using the RheoMetal process, Solid State Phenomena, 2013, vol. 192, pp. 392-397.

[16] L. Vozár, W. Hohenauer, Flash method of measuring the thermal diffusivity. A review, J. High Temperatures-High Pressures, 2004, 36(3), pp. 253-264.

[17] H. Fredriksson, U. Åkerlind. Physics of Functional Materials, John Wiley & Sons, NY, 2008.

[18] T. M. Tritt, Thermal Conductivity: Theory, Properties, and Applications, Kluwer Academic/Plenum, New York, 2004.

[19] Flotherm v. 10.1 user manual, Mentor Graphics Corporation ®, 2014.

[20] J. Antony, Design of Experiments for Engineers and Scientists, Elsevier Science & Technology Books, 2014.

[21] S. Ji, A. Das, Z. Fan, Solidification behavior of the remnant liquid in the sheared semisolid slurry of Sn–15 wt. % Pb alloy. Scr. Mater, 2002, 46(3), pp. 205-210.

[22] N. Saunders, The application of calculated phase equilibria to multi-component aluminum alloys, Journal of Japan Institute of Light Metals, 2001, 51(3), pp. 141-150.

[23] Z. Guo, W. Sha. Quantification of precipitate fraction in Al–Si–Cu alloys. Mater. Sci. Eng. A 392 (2005), pp. 449-452.

[24] H. Kaufmann, P. J. Uggowitzer. Metallurgy and Processing of High Integrity Light Metal Pressure Castings, Fachverlag Schiele & Schoen, Berlin, 2007.

[25] R. Rana, R. Purohit, S. Das, Reviews on the influences of alloying elements on the microstructure and mechanical properties of aluminum alloys and aluminum alloy composites. Int. J. Sci. Res. Publ., 2012, *2*(6), pp. 1-7.